The International Journal of Advanced Manufacturing Technology
https://doi.org/10.1007/s00170-025-15023-x

ORIGINAL ARTICLE

Advanced hybrid laminates: elastomer integration for optimized mechanical properties

Luca Raimondi[1,2] · **Federico Bernardi**[1]

Received: 17 August 2024 / Accepted: 6 January 2025

Abstract
Interleaving elastomeric films into polymeric composite materials is a promising technological solution to manufacture components with localized functionalities. To optimize processing time and reduce testing costs, there is an urgent need for modeling strategies to predict the effect of hybridization based on the fundamental properties of singular constituents. In this work, three different laminates with varying numbers and positions of elastomeric layers were manufactured and mechanically tested in flexural configuration. The digital image correlation (DIC) technique is employed to evaluate the displacements and the strain field on the surface of the sample. A numerical framework for the prediction of the mechanical response, including damage initiation and evolution, was developed and validated against experimental data. The numerical results showed significant agreement with the experiments, reporting a maximum mismatch of about 10% in strain distribution and about 2% in the ultimate load. Additionally, degradation trends in the load vs. deflection curves were always consistent. Analysis of the fractured surface and predicted failure modes further demonstrated the reliability of the method.

Keywords Hybrid polymer composite materials (HyPCM) · Elastomer interlayers · Mechanical testing · Progressive damage analysis

1 Introduction

The design and manufacturing of advanced composite structures have increasingly relied on polymeric composite materials (PCM) due to their customizable properties, versatility, and lightweight nature [1–3]. Among PCM, carbon fiber–reinforced polymers (CFRP) stand out for their superior mechanical properties, such as high strength-to-weight ratios, exceptional stiffness, and resistance to environmental degradation [4]. Despite their advantageous properties, CFRPs face significant challenges, including low interlaminar strength, poor residual resistance after impact, undesirable dynamic responses to vibrations [5], and inadequate damping properties. These limitations pose safety and regulatory concerns, particularly in critical structural applications. To address these challenges and enhance the functionality of composite structures, integrating elastomers (ELs)—flexible polymers known for their elasticity and energy dissipation properties—into CFRPs presents an established solution [6–10]. Liquid ELs, whether natural or synthetic, can be incorporated into the composite matrix to significantly improve the delamination toughness, impact resistance, and damping properties of a laminate [11]. Although this modification is easily achievable, it requires a specific resin formulation. Additionally, this change affects not only the bulk resin but also the entire component. This often results in reduced mechanical, thermal, and thermo-mechanical properties, along with a noticeable increase in weight [12]. A relatively new approach with the potential to tailor the local properties of a component involves the interleaving of thin mats composed of micro-sheets of ELs among the layers of conventional CFRP materials to form hybrid PCM (HyPCM) laminates. This type of modification can be virtually applied to any available commercial prepreg as the resin formulation is not altered. The idea of combining

✉ Luca Raimondi
luca.raimondi@unibo.it

[1] DIN - Department of Industrial Engineering - Alma Mater Studiorum, Università Di Bologna, Viale Risorgimento 2, 40136 Bologna, Italy

[2] CIRI-MAM - Interdepartmental Center for Industrial Research on Advanced Applications in Mechanical Engineering and Materials Technology - Alma Mater Studiorum, CIRI-MAM – Università di Bologna, Viale Risorgimento 2, 40136 Bologna, Italy

Published online: 16 January 2025

different polymers to manufacture HyPCM is not new in the literature. Liu et al. [13, 14] investigated the quasistatic crush behavior of hybrid unidirectional/woven carbon laminates both experimentally and numerically. Raimondi et al. [15] investigated the effect of combining different fiber architecture to form an hybrid laminate with improved tensile and flexural strength. Dhaliwal and Newaz [16] examined the damage response, energy absorption, and failure modes of fiber metal laminates (FML) by experimental and numerical studies. Massarwa et al. [17] and Acosta et al. [18] investigated the mechanical behavior of hybrid glass/carbon fiber composites under various loading conditions. Ahmed et al. [19] studied the impact response and failure of CFRP/Kevlar hybrid 3D woven panels under high-velocity impacts. Del Bianco et al. [20] performed an extensive experimental and numerical study on CFRP/flax hybrid laminates subjected to low-velocity impact tests. However, there are only a few works in the literature regarding numerical tools for predicting the elastic and fracture properties, and damage evolution of HyPCM laminates modified with EL films. Li et al. [21] performed experimental and numerical analyses to investigate the impact response and damage mechanisms of a hybrid carbon/elastomeric structure. Their study focused on the effects of protective rubber layer thickness strategically placed on the upper surface of test samples subjected to low-velocity impacts. Li et al. [22] conducted both numerical and experimental studies on the impact behavior of FML, utilizing rubber sheets as toughening layers between carbon and aluminum foils to improve adhesion in low-velocity impact tests. Albayrak et al. [23] explored the effects of stacking sequences and thicknesses of glass/elastomeric hybrid laminates on the impact energy absorption of a curved component. The investigation demonstrates that each stacking sequence necessitates the calibration of individual material parameters to fit experimental data. These studies focus on specific case analyses, which limits the ability to generalize the findings to situations where the position of the elastomeric film may vary. Several recent research demonstrated that by embedding elastomeric films in strategic regions of a CFRP laminate, it is possible to improve the interlaminar fracture toughness locally [24] to increment the energy absorption of CFRP in case of impact [25, 26], to improve damping [27, 28], to enhance adhesion between dissimilar materials [29, 30], or to create hinges for the manufacturing of integrated actuators in adaptive CFRP structures [31, 32]. Despite these attractive benefits, the effects of integrating soft EL films within the rigid structure of CFRP laminates dramatically transform the internal stress distribution [33, 34], which can trigger undesirable failure modes in the stiffer material [22, 35]. Advanced modeling techniques and comprehensive experimental validation are necessary to understand and control these behaviors [36], underscoring the need to fabricate multilayer components, determine their functionality, and simulate the behavior of new structures to validate the manufacturing procedure. Over the years, many damage models have been developed to predict the strength and failure modes of PCM [37–40], of which progressive damage models were most widely used [41]. The damage process of composites is primarily influenced by failure criteria and evolution methods. Initially, damage occurs in certain elements that meet the failure criteria. As this damage progresses, element failure begins to appear. Eventually, as the number of failed elements increases, the entire structure ultimately fails. Linde et al. [42] proposed a damage model to investigate the open-hole tensile progressive damage and failure mechanisms of fiber metal laminate. Although the strength was well predicted, only two failure modes can be obtained. El Idrissi et al. [43] studied the damage initiation and evolution of composite laminates in flexure. Their model accounted for intralaminar and interlaminar damage using Puck's criterion and cohesive zone modeling (CZM), demonstrating superior capability in predicting damage evolution compared to Linde's model. Yang et al. [44] proposed a progressive damage model based on a Hashin-type failure criterion and CZM to assess the flexural behavior of laminated composites subjected to three-point bending. This model considers eight possible failure modes and perfectly aligns with experimental load–deflection curves. In an attempt to provide a high-precision modeling approach for damaging CFRPs, Huang et al. [45] compared different failure criteria (Hashin/Puck), evolution methods (sudden/linear/exponential), and interface models (zero-thickness cohesive elements/finite-thickness cohesive elements/cohesive contact). From their investigation, it was found that the accuracy of the simulation was mainly influenced by the adopted interface model rather than failure criteria or evolution method. It can be concluded that an appropriate characterization and modeling of the interface are essential to provide trustable results in numerical simulations.

In this work, the effects of integrating different numbers and positions of elastomeric films into CFRP structures were experimentally and numerically evaluated to understand their impact on the variation of flexural and fracture properties at both the local and global levels. Different types of laminates were produced, in which both the effect of increasing the number of interfaces and their positioning were considered representative of the main processing challenges. A general numerical environment based on a Hashin-type failure criterion with exponential degradation was integrated through a user-defined material subroutine (UMAT) to capture intra-laminar damage initiation and evolution accurately in CFRP/PCM material. Interlayers were modeled with finite thickness elements to capture interlaminar damage phenomena accurately. The different configurations of laminates were mechanically tested and used for two separate experiments: the first aimed at

determining the accuracy of the numerical model in predicting displacements and deformations and the second to identify the failure and progressive damage of the modified laminates.

2 Material and methods

PCM and elastomeric materials used in this work are presented in Section 2.1, together with methods used for the characterization of their individual mechanical properties. Section 2.1.3 describes the manufacturing methods used for the preparation of HyPCM laminates and the methodology used to extract samples for mechanical testing. Methodologies for mechanical testing are illustrated in Section 2.2. Methods used to implement the numerical model are presented in Section 2.3.

2.1 Constituent material characterization and manufacturing of HyPCM laminates

2.1.1 PCM

The PCM used in this work was a unidirectional prepreg provided by Delta-tech (Delta Tech S.p.A, Altopascio, Italy). It consists of Toray T700S high-strength carbon fibers impregnated with 40% (V_m) DT120 high-toughness epoxy resin. The areal weight of the tape was 300 g/m^2, and the nominal cured ply thickness was 0.322 mm ± 0.4% (averaged from 3 manufactured plates). Tensile tests for 0° and 90° were conducted according to ASTM standard D3039 [46]. The in-plane shear response of the material was characterized by loading in tensile a ± 45° laminate according to ASTM standard D3518 [47], and the DIC technique was used to evaluate the strains.

2.1.2 Elastomeric film

The elastomeric interface film layer used in this work is Kraibon AA6CFZ, with an average thickness of 360 µm and density of 1030 kg/m^3, provided by Gummiwerk KRAIBURG GmbH & Co. KG (Waldkraiburg, Germany). The mixture is ethylene-propylene-diene monomer (EPDM) rubber elastomers, which have the benefit of providing excellent adhesion to the epoxy matrix. The elastomer is supplied pre-cured and vulcanizes during the autoclave process as CFRP. Tensile tests of vulcanized material were carried out following the protocol described in Section S1 of the Supplementary Information.

2.1.3 HyPCM manufacturing and sample preparation

Hybrid laminates were prepared via hand lay-up in an air-conditioned clean room (21 °C, 26% relative humidity). The elastomeric film was interleaved during lamination by directly applying patches, supported by their becker, on the wet prepreg. Supporting film was then removed before adding other prepreg plies. Four different layup configurations were produced with an increasing number of modified layers, as depicted in Fig. 1. All laminates were cured in an autoclave for 2 h at a temperature of 135 °C, 6 bar external pressure, with a heating/cooling ramp of 2 °C/min. After curing, specimens were diamond saw cut from the respective laminate plates and checked for imperfections. Samples for the mechanical characterization were 192 mm long and

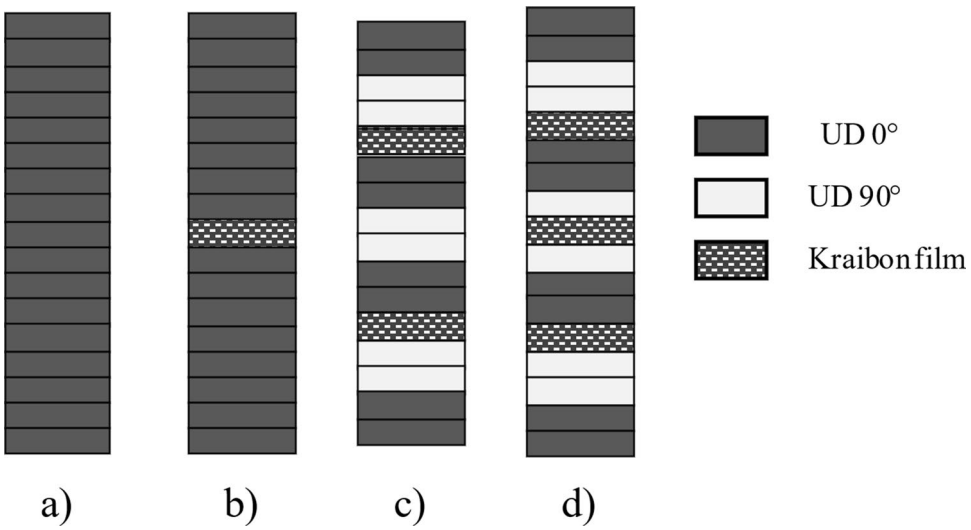

Fig. 1 **a** configuration L0 [0_{16}]; **b** configuration L1 [0_8;K;0_8]; **c** configuration L2 [0_2;90_2;K;0_2;90_2;0_2;K;90_2;0_2]; **d** configuration L3 [0_2;90_2;K;0_2;90;K;90;0_2;K;90_2;0_2]

10 mm in depth (averaged from 3 measurements on each specimen). A white-on-black speckle pattern was applied on the lateral surface of the flexural specimens with a spray can. Care was taken in optimizing the size and distribution of pattern features to meet the optimal density of 50% suggested in [48] and the optimal size of 3–5 pixels per dot indicated by [49], resulting in an optimal size of features in the range 35–58 [μm] for the measurement setup used in this work.

2.2 Mechanical characterization

Flexural samples were monotonically loaded in a three-point bending (3 PB) configuration at a 2 mm/min test rate into an Instron 8033 universal testing machine equipped with a 2 kN load cell. A fixed 1/32 support span-to-thickness ratio was assumed for all specimens. To mitigate inaccurate measurements caused by potential variations in width and thickness between samples, flexural stress (Eq. (1)) and strain (Eq. (2)) was calculated following the recommendation of ASTM D790-10 standard [50]:

$$\sigma_f = \frac{3PL}{2bd^2} \tag{1}$$

and

$$\varepsilon_f = \frac{6Dd}{L^2} \tag{2}$$

Being P the load recorded by the load cell, D the crosshead displacement, b the width of the sample, L the span, and d the sample thickness. The strain and stress describe the fictional values for a homogeneous material with the same flexural characteristics. The specimens were monitored during loading at a frequency of 2 Hz using a 5-megapixel camera (2440×2050, 8-bit, black-and-white) from a commercial DIC system (Q400, Dantec Dynamics, Skovlunde Denmark). The camera was equipped with a high-quality metrology-standard 35 mm lens (Apo-Xenoplan 1.8/35, Schneider – Kreuznach, Germany; 135 mm equivalent), and the specific configuration used resulted in a spatial resolution of 87 pixels per millimeter. The acquired images were post-processed using GOM Correlate 2022, developed by GOM GmbH in Braunschweig, Germany (accessible via https://www.gom.com/). The correlation parameters were set as follows: facet size of 15 pixels, point distance of 7 pixels, and temporal filter (median) set to 3 to achieve a correlation accuracy of 0.1 pixels. The experimental setup configuration is shown in Fig. 2.

2.3 Numerical simulation

2.3.1 FEA model

Abaqus/Standard 2023 with an implicit solver was adopted to simulate the bending behavior of the different laminates. The specimens from laminate L0 and L2 were modeled with 16 solid volumes, each representing a layer of the composite material or elastomeric film, while 17 solid volumes were used to model samples from laminates L1 and L3. The PCM material was modeled using 8-node three-dimensional solid elements with reduced integration (C3D8R), whereas a hybrid version (C3D8RH) was used for the rubber material. An enhanced stiffness control method was adopted to mitigate the hourglass effect resulting from reduced integrated elements. The nose and the loading supports were modeled as discrete rigid body elements (R3D4) featuring a mesh density of 0.5 mm. The penalty contact method is used to describe the tangential contact behavior between samples, the nose, and loading supports, with a friction coefficient of $\mu = 0.2$ [51]. The normal behavior is defined using the hard contact algorithm to prevent the penetration of the contacting surfaces. A mesh convergence study was conducted on samples from laminate L0, with the in-plane element size varied from 0.5 to 2 mm, as illustrated in Fig. 3.

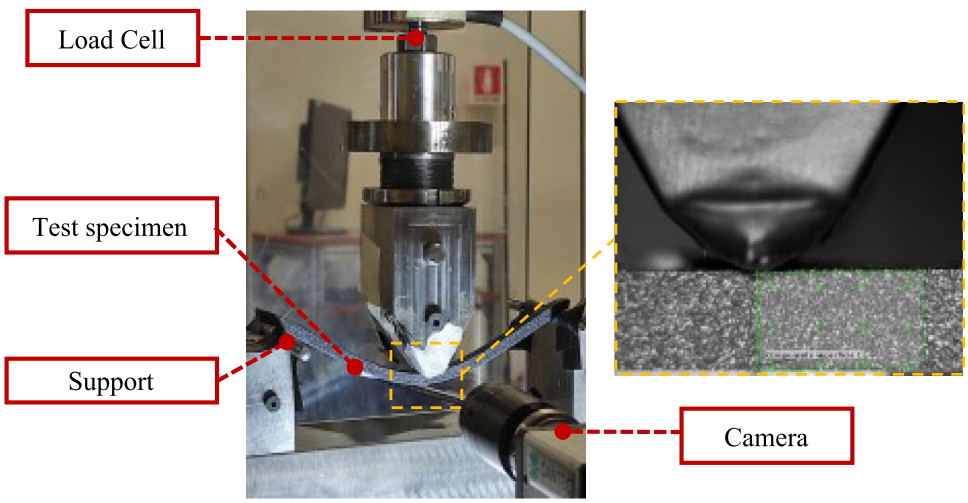

Fig. 2 Experimental setup configuration

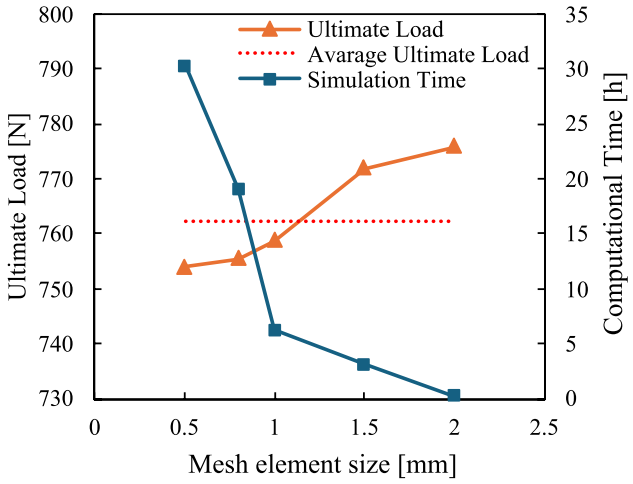

Fig. 3 Mesh convergency study for the in-plane element density

An in-plane mesh density of 1 mm was selected to balance between computational accuracy (0.48% error in the averaged ultimate load) and computational time (6 h on an Intel i7 processor with 16 CPUs). It is worth mentioning that the mesh size is not necessarily constant for modeling the three-point bending. Biased meshing could significantly reduce the computational time while ensuring sufficiently fine mesh where the delamination may occur. As delamination sites are hard to be predicted a priori in large applications, several adaptive mesh refinement (AMR) techniques have been developed to optimize computational cost. This approach to dynamic refinement enhances the accuracy of stress and strain predictions, supports the monitoring of evolving damage patterns, and enables the examination of larger and more complex structural systems [52, 53]. While AMR offers a potential for improving computational efficiency in modeling damage in composite laminates, it presents challenges such as implementation complexity, increased memory demands, sensitivity to refinement criteria, and potential mesh quality issues. Therefore, while this study adopts a constant mesh size approach to advance the understanding of damage mechanisms in HyPCM laminates, the potential of manual or automatic refining techniques like AMR remains an interesting avenue for future exploration.

Additionally, the chosen through-thickness element size ensures the presence of three elements per layer, adhering to the study's requirements for detailed analysis. The definition

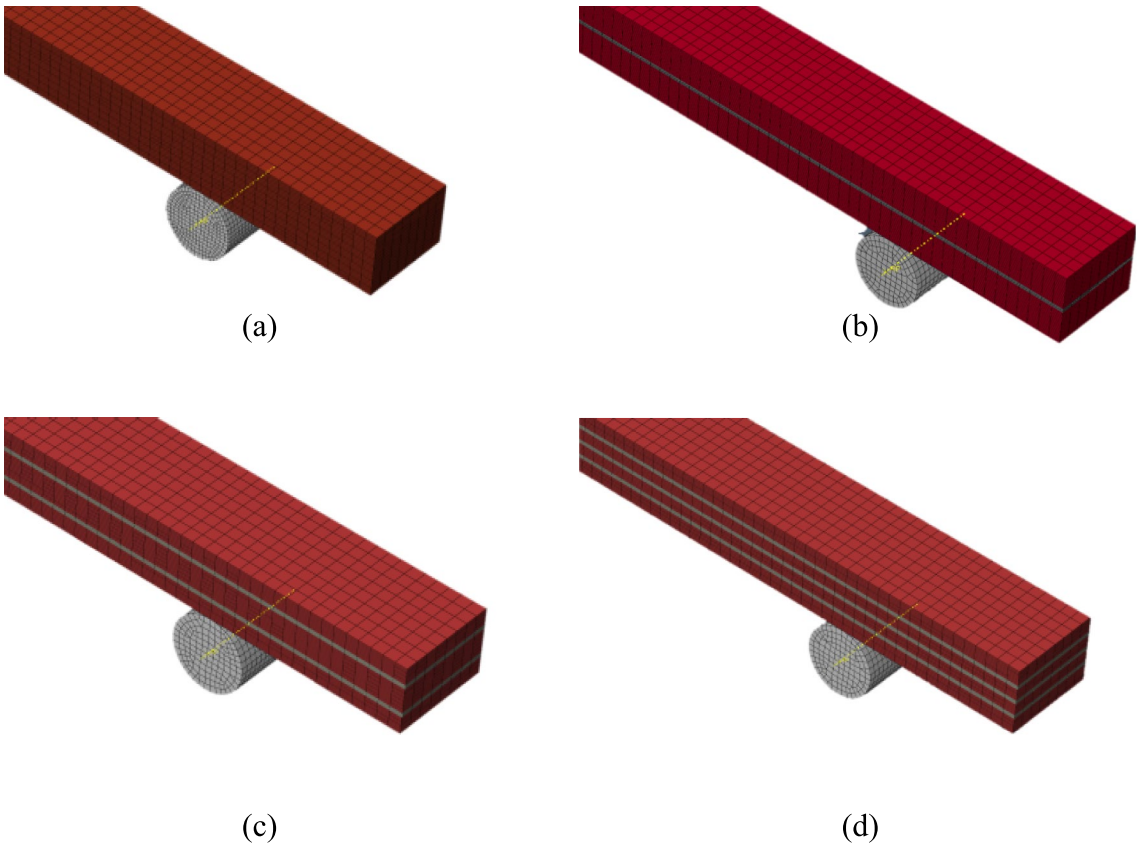

Fig. 4 Definition of the optimized mesh scheme for both the reference and the 3 HEEML laminates in the flexure test. **a** Configuration L0 [0_{16}], **b** configuration L1 [0_8;K;0_8], **c** configuration L2 [0_2;90_2;K;0_2;90_2;0_2;K;90_2;0_2], **d** configuration L3 [0_2;90_2;K;0_2;90;K;90;0_2;K;90_2;0_2]

Table 1 Material properties of PCM material

Material property	Value	Units
Density	$\rho = 1500$	kg/m^3
Elastic properties	$E_1 = 104{,}000$	MPa
	$E_2 = 6884$	MPa
	$E_3 = 6884$	MPa
	$\nu_{12} = 0.36$	-
	$\nu_{13} = 0.36$	-
	$\nu_{23} = 0.45$	-
	$G_{12} = 2395$	MPa
	$G_{13} = 2395$	MPa
	$G_{23} = 4950$	MPa
Strength	$X_T = 1610$	MPa
	$X_C = 820$	MPa
	$Y_T = 26$	MPa
	$Y_C = 52$	MPa
	Z_T=26	MPa
	$Z_C = 52$	MPa
Fracture energies [56]	$G_f = 22.5$	N/mm
	$G_m = 1.6$	N/mm

of the optimized mesh scheme for samples considered in this work is given in Fig. 4.

2.3.2 Material models for numerical analysis

To capture the complex interplay phenomena that occur between the elastomeric film and the PCM under loading, a nonlinear material model based on progressive damage of the composite material was adopted through a user-defined material subroutine (UMAT). Linear orthotropic elasticity was employed in the UMAT to model the intra-laminar mechanical behavior of the PCM material up to failure. A full 3-dimensional Hashin-type failure criterion [44] was adopted to predict intralaminar damage initiation. Seven possible failure modes were considered, namely fiber tensile (FT) and fiber compression (FC), in-plane matrix cracking (IMT) and crushing (IMC), out-of-plane matrix cracking (OMT), and out-of-plane matrix crushing (OMC) expressed by:

Fiber tension (FT) if $\varepsilon_1 > 0$:

$$s_{FT}^2 = \left(\frac{\varepsilon_1}{X_t/C_{11}}\right)^2 + \left(\frac{\gamma_{12}}{S_{12}/C_{44}}\right)^2 + \left(\frac{\gamma_{13}}{S_{13}/C_{55}}\right)^2 \quad (3)$$

Fiber compression (FC) if $\varepsilon_1 < 0$:

$$s_{FC}^2 = \left(\frac{\varepsilon_1}{X_c/C_{11}}\right)^2 \quad (4)$$

In-plane matrix cracking (IMT) if $\varepsilon_2 > 0$:

$$s_{IMT}^2 = \left(\frac{\varepsilon_2}{Y_t/C_{22}}\right)^2 + \left(\frac{\gamma_{12}}{S_{12}/C_{44}}\right)^2 + \left(\frac{\gamma_{23}}{S_{23}/C_{66}}\right)^2 \quad (5)$$

In-plane matrix crushing (IMC) if $\varepsilon_2 < 0$:

$$s_{IMC}^2 = \left(\frac{\varepsilon_2}{Y_c/C_{22}}\right)^2 + \left(\frac{\gamma_{12}}{S_{12}/C_{44}}\right)^2 + \left(\frac{\gamma_{23}}{S_{13}/C_{66}}\right)^2 \quad (6)$$

Out-of-plane matrix cracking (OMT) if $\varepsilon_3 > 0$:

$$s_{OMT}^2 = \left(\frac{\varepsilon_3}{Z_T/C_{33}}\right)^2 + \left(\frac{\gamma_{13}}{S_{13}/C_{55}}\right)^2 + \left(\frac{\gamma_{23}}{S_{23}/C_{66}}\right)^2 \quad (7)$$

Out-of-plane matrix crushing (OMC) if $\varepsilon_3 < 0$:

$$s_{OMC}^2 = \left(\frac{\varepsilon_3}{Z_c/C_{33}}\right)^2 + \left(\frac{\gamma_{13}}{S_{13}/C_{55}}\right)^2 + \left(\frac{\gamma_{23}}{S_{23}/C_{66}}\right)^2 \quad (8)$$

where $\varepsilon_i (i = 1,2,3)$ and $\sigma_i (i = 1,2,3)$ are respectively the normal strain and stresses and $\tau_{ij} (i,j = 1,2,3 i \neq j)$ the shear stresses. X_T, Y_T, and Z_T are the ultimate tensile strength along longitudinal, transversal, and trough-thickness directions respectively. X_C, Y_C, and Z_C are the ultimate compressive loads in compression along the same directions while S_{12}, S_{13}, and S_{23} are the longitudinal, transversal, and trough thickness shear strengths. The flow chart of the UMAT is reported in Supplementary Information, Section S2. The values of elasticity and strength for the PCM material were derived from the results of quasi-static tests and reported in Table 1. A continuum damage mechanics (CDM) approach is employed to capture the intralaminar damage evolution [44]. The effect of damage is described by reducing the value of stiffness components of the element [54]:

$$C_{ij}^d = \left(1 - d_k\right) C_{ij}^0 \quad (9)$$

Here C_{ij}^0 (i, j = 1, 2, 3, 4, 5, 6; i = j) are the initial stiffness components of the element, while C_{ij}^d (i, j = 1, 2, 3, 4, 5, 6; i = j) denote the final stiffnesses after damage initiation. The 6 damage parameters d_k (k = FT, FC, IMT, IMC, OMT, OMC) are calculated as a function of the stiffness components C_{ij} and strain ε_i after damage initiation [55] and monotonically increase from 0 (no damage) to 1 (fully damaged) according to the relationship [44]:

Table 2 Material properties of the cohesive interface

Material property	Value	Units
K_n	34500	MPa/mm
$K_s = K_t$	3450	MPa/mm
t_n^0	12.8	MPa
$t_s^0 = t_t^0$	24.2	MPa
G_{IC}	0.452	N/mm
$G_{I/C}$	1.549	N/mm
η	1	-

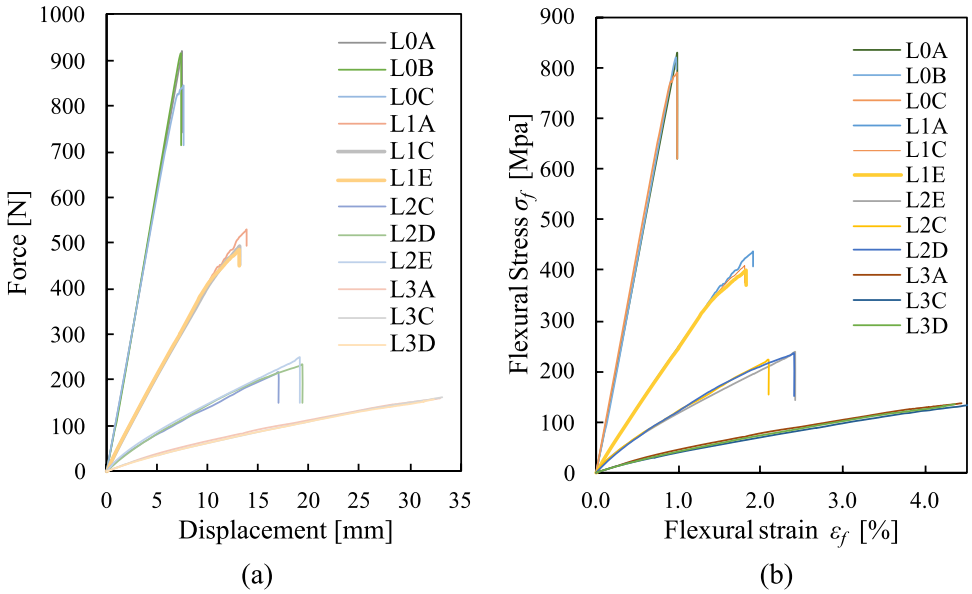

Fig. 5 Results from experimental tests. **a** Load–deflection curves for the 4 laminates (L0, L1, L2, L3), **b** Flexural stress–strain curves for the 4 laminates (L0, L1, L2, L3). Strain and flexural stress are calculated for the outer fiber of a homogeneous material

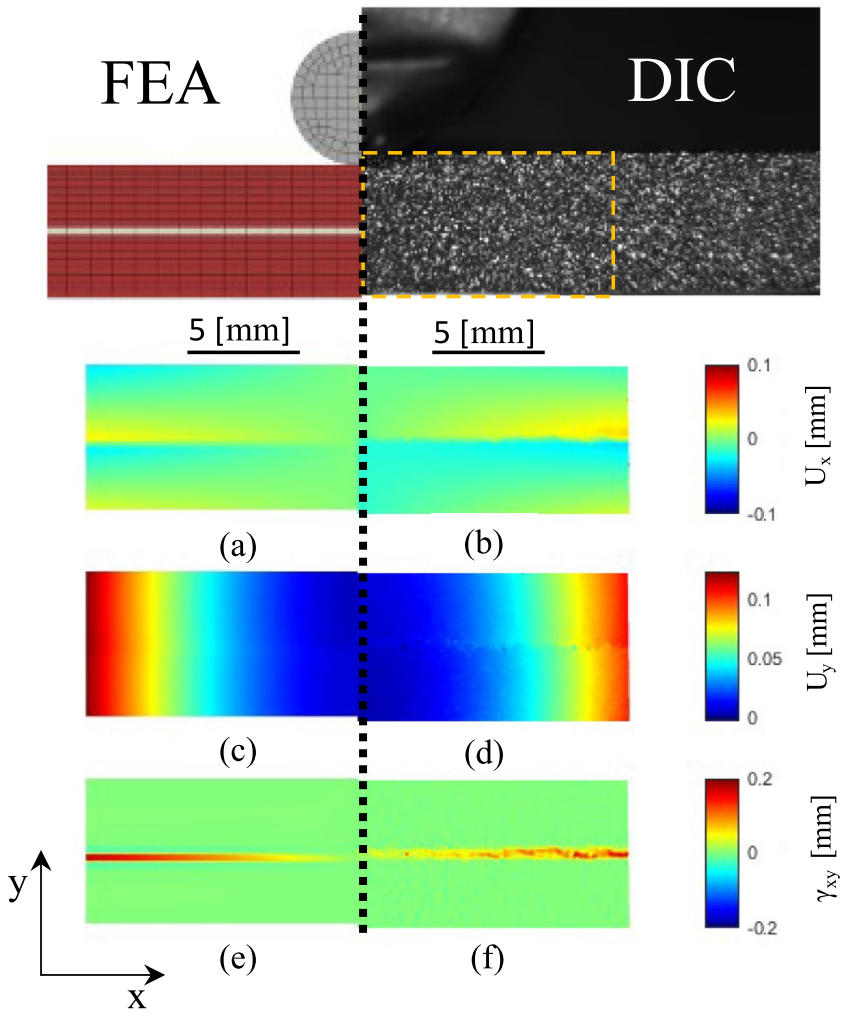

Fig. 6 Displacements and shear strain distribution for laminate L1 at mid-span on the side surface captured at 30% of failure load. (a) Horizontal displacement U_x calculated by FEA, (b) horizontal displacement U_x measured by DIC, (c) vertical displacement U_x calculated by FEA, (c) vertical displacement U_y calculated by FEA, (d) vertical displacement U_y measured by DIC, (e) shear strain γ_{xy} calculated by FEA, (f) shear strain γ_{xy} measured by DIC

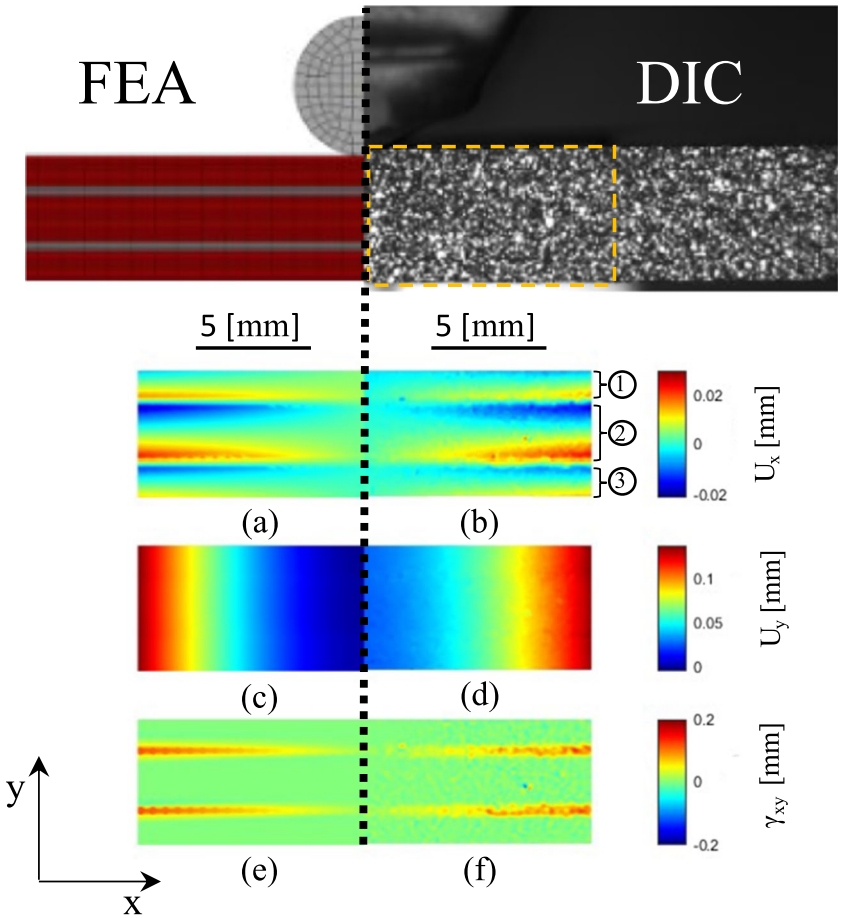

Fig. 7 Displacements and shear strain distribution for laminate L2 at mid-span on the side surface captured at 30% of failure load. (a) Horizontal displacement U_x calculated by FEA, (b) horizontal displacement U_x measured by DIC, (c) vertical displacement U_x calculated by FEA, (c) vertical displacement U_y calculated by FEA, (d) vertical displacement U_y measured by DIC, (e) shear strain γ_{xy} calculated by FEA, (f) shear strain γ_{xy} measured by DIC

$$d_k = 1 - \frac{1}{s_k} exp\left(\frac{C_{ij}\varepsilon_i^2(1-s_k)L^C}{G_k}\right) \tag{10}$$

Here G_k is the fracture energy of the matrix or the fiber depending on the failure mode and L^C the characteristic length of the element. As reported by Linde et al. [42], the use of L^C and G_k helps in minimizing mesh sensitivity of numerical results, which is a common problem for material with strain softening response.

Several strain energy potentials in Abaqus/standard demonstrate good stability within the strain range of the experimental dataset presented in Section S1. These include Neo Hooke (reduced polynomial, $N=1$), Yeoh (reduced polynomial, $N=3$), Arruda-Boyce, and Marlow models. After comparing these potentials, the Marlow [57] model was selected for its superior accuracy in fitting the stress–strain curve of the rubber interlayer. According to Marlow, the strain energy density function can be expressed as:

$$U = U_{dev}\left(\bar{I}_1\right) + U_{vol}\left(J_{el}\right) \tag{11}$$

Being U the strain energy per unit volume, U_{dev} the deviatoric part, U_{vol} the volumetric part, $\bar{I}_1$ the first deviatoric strain invariant, and J_{el} the volume ratio. U_{dev} was calculated directly from testing data (see Section S1 of the Supplementary Information). For the compressive behavior, the volumetric part U_{vol} is defined by the Poisson ratio of 0.49.

2.3.3 Delamination models

To accurately capture interlaminar delamination, a cohesive zone model (CZM) was employed at the interface of each PCM volume [58, 59]. Bilinear cohesive elements (COH3D8) with 0.001 mm finite-thickness were used to reflect the actual thickness of the epoxy interlayers. The elastic behavior of the CZM material was modeled through the relationship:

$$\boldsymbol{t} = \begin{Bmatrix} t_n \\ t_s \\ t_t \end{Bmatrix} = \begin{pmatrix} K_n & 0 & 0 \\ 0 & K_s & 0 \\ 0 & 0 & K_t \end{pmatrix} \begin{Bmatrix} \delta_n \\ \delta_s \\ \delta_t \end{Bmatrix} \tag{12}$$

being $\boldsymbol{t}$ the nominal traction stress vector representing the stress induced by the three deformation modes: the deformation in the normal direction δ_n and two shear deformation modes δ_s and δ_t. The quadratic failure criterion and the

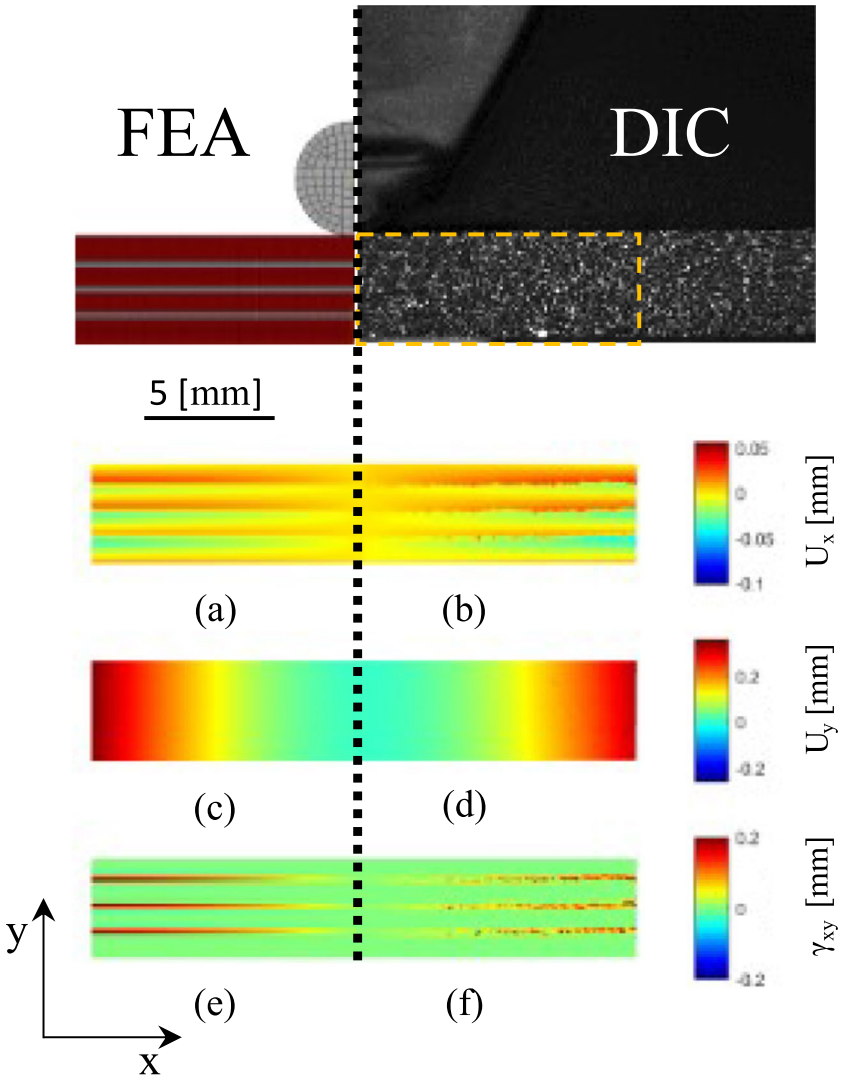

Fig. 8 Displacements and shear strain distribution for laminate L3 at mid-span on the side surface captured at 30% of maximum recorded load. (a) Horizontal displacement U_x calculated by FEA, (b) horizontal displacement U_x measured by DIC, (c) vertical displacement U_x calculated by FEA, (c) vertical displacement U_y calculated by FEA, (d) vertical displacement U_y measured by DIC, (e) shear strain γ_{xy} calculated by FEA (f) shear strain γ_{xy} measured by DIC

Benzeggagh–Kenane (BK) law [60] are employed to predict the initiation and propagation of delamination damage, expressed in Eqs. (11) and (12) respectively:

$$\left\{\frac{\langle t_n\rangle}{t_n^0}\right\}^2+\left\{\frac{t_s}{t_s^0}\right\}^2+\left\{\frac{t_t}{t_t^0}\right\}^2=1 \tag{13}$$

where t_n^0, t_s^0, and t_t^0 are the peak values of the nominal stress of the interface when separation is merely aligned with the respective fracture mode.

$$G_C=G_{IC}+\left(G_{IIC}-G_{IC}\right)\left(\frac{G_{II}+G_{III}}{G_I+G_{II}+G_{III}}\right)^{\eta} \tag{14}$$

Being G_C, G_{IC}, and G_{IIC} respectively the total, normal, and shear critical fracture energies and G_I, G_{II}, and G_{III} the energy release rate under Mode I, Mode II, and Mode III respectively. η is the relevant material parameter in the BK law [56, 61]. Calibrated parameters for the inter-laminar material model are reported in Table 2 for a mesh size of 1 mm.

Failure in the interfaces between PCM and the elastomeric layer was not modeled, as no delamination was observed in the experimental tests.

3 Result and discussion

3.1 Mechanical characterization

Results from flexural tests are presented in Fig. 5, where the curves of each laminate of the bending experiments are visualized. Good repeatability was found across all samples, with the CV value of maximum flexural stress at break consistently lower than 5% for all L0, L1, and L2 samples.

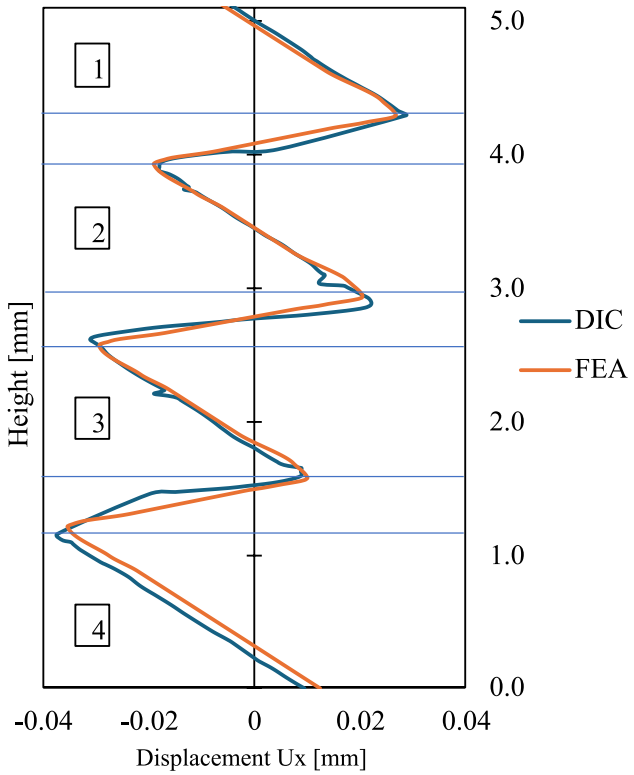

Fig. 9 Horizontal displacement field U_x for a representative L3 sample

Among the laminates tested, L0 exhibited the highest stiffness and strength, followed by laminates L1, L2, and L3. The strains to failure were contrary to the strength. Samples from laminates L0, L1, and L2 experienced failure at the midpoint between the supports. The mechanical characterization tests for specimens from laminate L3 were terminated at a crosshead stroke of 33 mm due physical constraints of the testing equipment used. Laminates with fewer EL layers, such as L1 (one EL layer), retain more of CFRP's inherent stiffness, while configurations like L2 and L3, with multiple EL layers, demonstrate higher compliance.

This added flexibility enables these configurations to accommodate greater strain, though with a reduction in stiffness and strength. Both force vs. displacement (Fig. 5a) and stress–strain curves (Fig. 5b) for the laminate L0 were linear up to 98% of the ultimate strength. In contrast, stress–strain curves for laminate L1 were linear up to 90% of the ultimate strain, with an acceptable reduction of 10% in the measured flexural modulus. Afterward, as strain increased, stresses rose slowly and then abruptly declined due to fracture (see Fig. 5b). Configurations L2 and L3 exhibited highly nonlinear stress–strain behavior with marked strain-hardening effects. It can be argued that the inclusion of EL layers within the laminates modifies the internal stress distribution and load-bearing capability. EL layers likely provide energy dissipation via shear deformation at the CFRP interface—a point that later DIC and FEA analyses are expected to confirm—by altering the shear transfer between CFRP layers.

This effect might explain the strain-hardening behavior observed in these configurations, where L2 showed a reduction in flexural modulus by approximately 28% at 30% of the ultimate strain, 41% at 50%, and 44% at 75%. For laminate L3, reductions were around 18%, 28%, and 35% at 30%, 50%, and 75% of the maximum recorded strain, respectively.

3.2 DIC results and numerical model validation

The DIC technique offered considerable insights into elucidating the role of the interlayer in the global deformation mechanisms of the various laminates investigated in this study. Nevertheless, the exploration of the behavior of the multi-material beams with high resolution necessitated the magnification of the images of the surfaces, which, in turn, constricted the depth of field [62, 63]. Correlation was feasible within a window approximately 10 mm × 10 mm, wherein both focus and contrast were observed to be optimal. At midspan, under the nose, horizontal displacement U_x was null for all samples due to symmetry in load and material (see Figs. 6b, 7b, and 8b). In laminate L1, at a small distance from the midspan, the distribution of the horizontal component of the displacement field within the sample highlights the formation of two distinct deformable regions (Fig. 6b) separated by the EL interlayer. As visible in Fig. 6a, in which FEA results are displayed, the phenomenon is correctly captured by the numerical model, with a maximum mismatch of 7 µm.

The vertical displacement U_y was null at midspan and maximum along the border of the region of interest in both experimental measurements (Fig. 6d) and numerical results (Fig. 6c). Experimental shear strain distribution γ_{xy} over the surface of a representative L1 sample is illustrated in Fig. 6f. Shear deformation in the rubber interlayer approached the minimum at midspan and the maximum along the horizontal axis at the outer part of the region under investigation. At this loading step, a maximum of 20% in shear deformation within the elastomeric film and a 0.2% shear deformation in the PCM material were measured. Numerical results, illustrated in Fig. 6e, were in good accordance with experimental ones, with an averaged mismatch of 10–15% within the rubber. For L1 samples, measurements for ε_x and ε_y fell within the precision of the DIC measurements [62], and a comparison with FEA was not feasible.

For a representative sample from laminate L2, measurements of the horizontal component of the displacement field highlight the presence of 3 regions (1, 2, and 3 in Fig. 7b) with distinct deformation patterns. At a small distance from

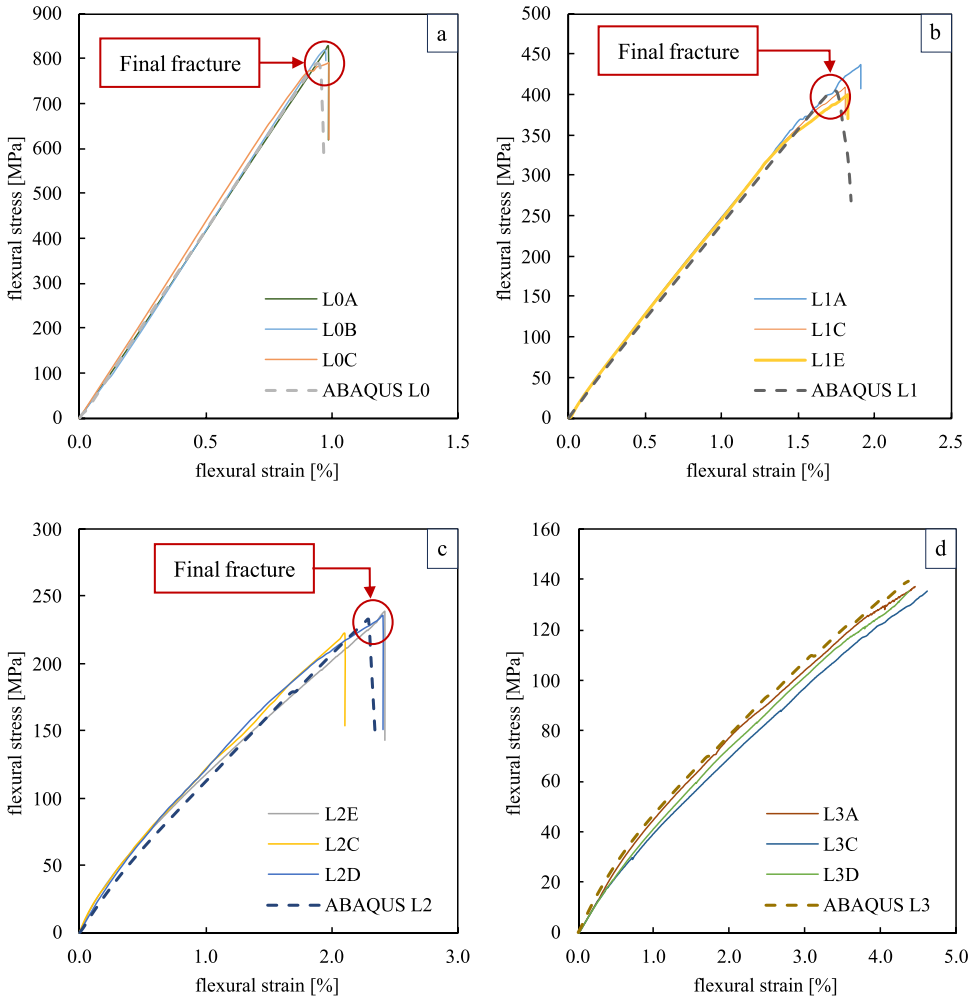

Fig. 10 Comparison between experimental flexural stress–strain curves (solid lines) and numerical predictions (dashed lines). **a** Laminate L0, **b** laminate L1, **c** laminate L2, **d** laminate L3

the nose, the specimen's top outer fibers (within Region 1) are negatively elongated, contrasting with the bottom outer fibers in Region 3, which are positively elongated. Despite the opposite nature of these elongations, their magnitudes were closely matched. No horizontal displacement was measured at the centerline of the specimen, suggesting that this region acts as a neutral axis for deformation in region 2. Maximum absolute longitudinal elongations were measured in Region 2 at the interface between the PCM material and the elastomeric film. Numerical results, depicted in Fig. 8a, were in excellent agreement with experimental findings, with a maximum scatter of 2 µm. Experimental shear strain measurements (Fig. 8f) were consistent with FEA (Fig. 8e), with an average mismatch of 13–15% within the rubber.

After increasing the number of rubber interfaces to 3, a more complex deformation pattern was observed. Analysis of a representative sample of the L3 laminate revealed that the horizontal displacement field measurements, illustrated in Fig. 8b, show four characteristic zones, each characterized by its own unique pattern. Also for this configuration, numerical results for the horizontal displacement field (Fig. 8a) were highly consistent with experimental data. Thanks to the high signal-to-noise ratio, both numerical (Fig. 8d) and measured values (Fig. 8c) for the vertical displacements overlap, with an average difference in the range of about 1 µm. Experimental shear strain measurements (Fig. 8f) were consistent with FEA (Fig. 8e), with an average mismatch of 10–15% within the rubber. Displacement distribution U_x for a section close to the border is given in Fig. 9. Outer fibers of the laminate showed moderate horizontal displacement: the top outer fibers of the specimen were negatively elongated, while the bottom outer fibers were positively elongated. Maximum positive elongation was detected in Region 1 of Fig. 9 at the interface between PCM and the elastomeric film, while minimum elongation was detected in Region 4 of Fig. 9 at the interface between PCM and the rubber. Elongations in Regions 2 and 3 of Fig. 9 were less pronounced. The minimum consistently occurred at the upper side of those regions, while the maximum occurred at the lower side. This behavior is opposite in sign to what was

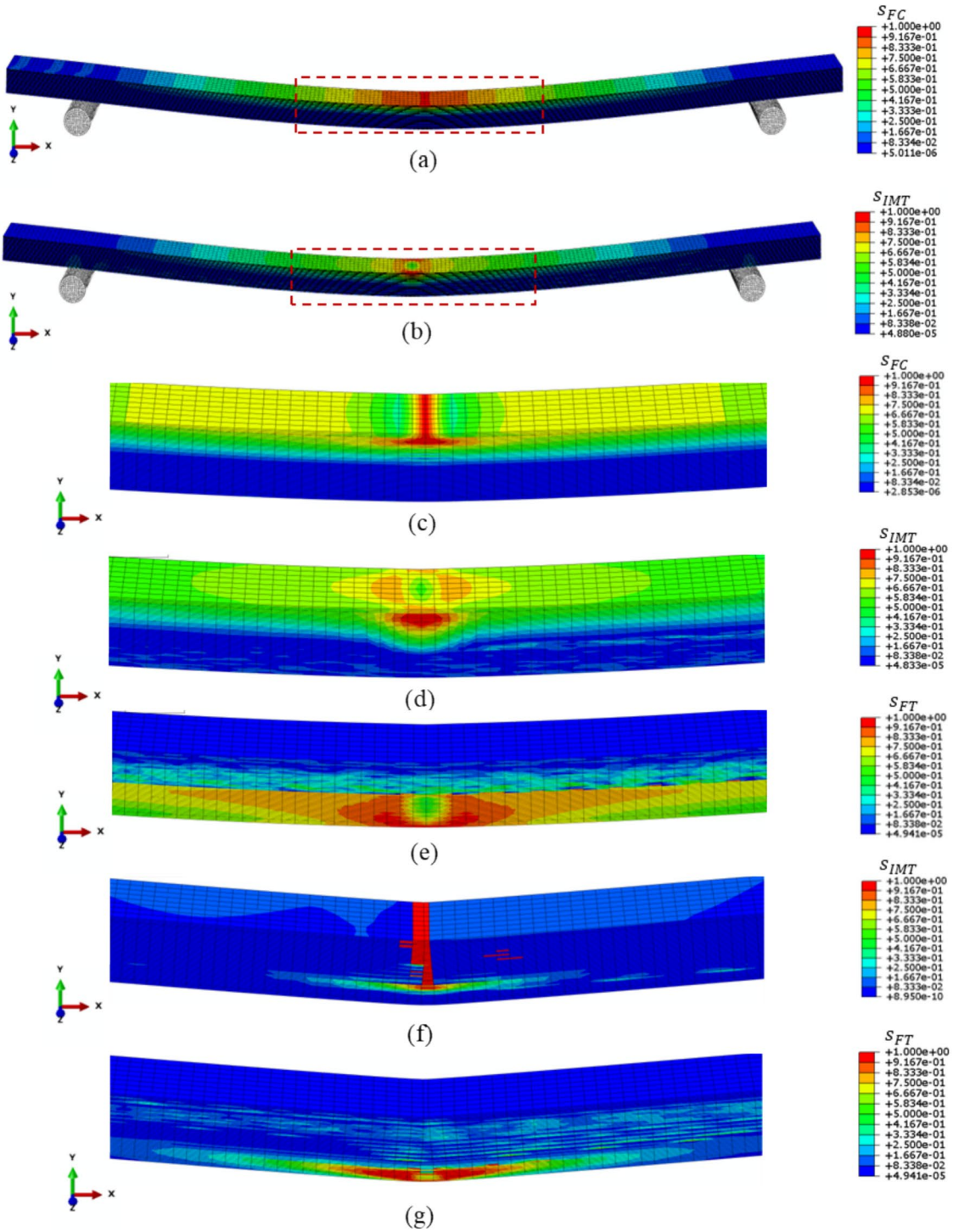

Fig. 11 Failure initiation and damage progression for L0 laminate. **a** Contour for s_{FC} (fiber compression) at 99% of ultimate load, **b** contour for s_{IMT} (in-plane matrix cracking) at 99% of ultimate load, **c** contour for s_{FC} (fiber compression) after failure, **d** contour for s_{IMT} (in-plane matrix cracking) after failure, **e** contour for s_{FT} (fiber tensile) after failure, **f** contour for s_{IMT} (in-plane matrix cracking) after complete degradation, **g** contour for s_{FT} (fiber tensile) after complete degradation

measured in the L1 samples. The reversal in sign in the L3 laminate is likely due to the significant interaction between Regions 1 and 2, and Regions 3 and 4 thanks to the high toughness and deformability of the interlayer.

Upon comparing the outcomes from L2 and L3 samples, it can be argued that the interfaces between the external layers of these laminates hold critical importance for the structural integrity of the part.

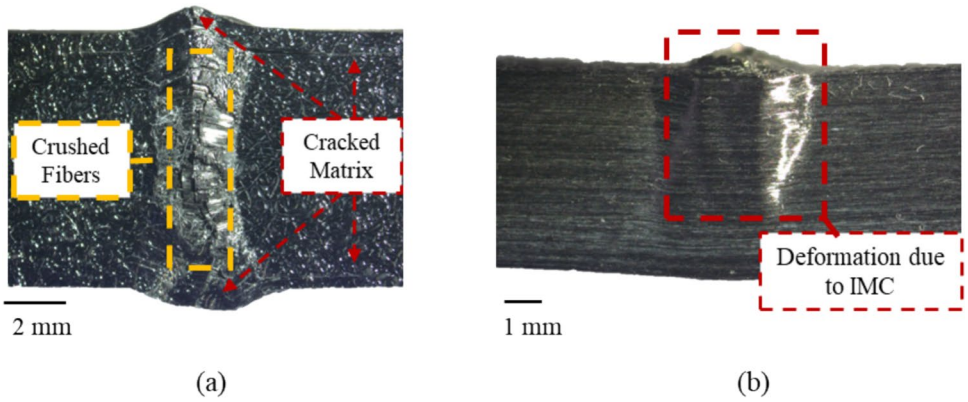

Fig. 12 Surfaces of an L0 sample at midspan. **a** Top surface, **b** lateral surface

3.3 FEA and failure analysis

Experimental flexural stress-displacement curves for all laminates investigated are compared with numerical predictions in Fig. 10. For all configurations, the numerical model could properly capture the deformation characteristics of each laminate, with minor scatter for laminate L2 (Fig. 10c) and laminate L3 (Fig. 10d). The maximum ultimate flexural strength predicted by FEA was always within the experimental variability.

To assess the model's ability to adequately capture the failure mechanisms of different laminates and to predict their damage evolution, analysis of failure parameters, at (i) 99% of the ultimate load, (ii) during propagation, and (iii) at the end of simulations, was performed.

Analysis of samples from laminate L0 is illustrated in Fig. 11. At 99% of the ultimate load, an $s_{FC} = 1$ was approached at the upper surface under the nose (ply 1), indicating incipient fiber failure in compression (Fig. 11a).

At the same load step, as illustrated in Fig. 11b, incipient in-plane matrix cracking was predicted at the edges of the upper surface under the nose (ply 1), where the s_{IMT} parameter equals one. All other failure parameters were lower than the threshold at this stage. After the first degradation, fiber failure in compression and in-plane matrix cracking progressively propagates through the thickness of the laminate, as shown in Fig. 11 c and d. At this stage, incipient fiber breakage in tensile is detected on the bottom surface of the sample in ply 16 (Fig. 11e). At the end of the simulation, Fig. 11f, consistent matrix crushing was visible across a wide range of the sample thickness (plies 1–14). Fiber failure in tensile was predicted in the lower surface of the sample (ply 15 and ply 16), as illustrated in Fig. 11g. The top and lateral surfaces of a tested L0 sample at midspan are illustrated in Fig. 12.

The top surface of the sample, as depicted in Fig. 12a, exhibited a significant area degraded by in-plane matrix cracking [43], evidenced by the presence of discernible cracks and permanent deformation centrally located. This permanent deformation was observable as a V-shaped distortion on the side surface of every specimen tested, extending approximately 80% of the sample's thickness, as illustrated in Fig. 12b. The failure path was symmetric with respect to the axis of the loading nose. Fiber crushing was markedly observable at the center of the top surface (Fig. 12a), where the accumulation of degraded material caused the emersion of broken fiber tows. These findings overlap with the numerical predictions of Fig. 11f, demonstrating the high accuracy of the numerical model [64] in accurately predicting the damage evolution. Consistently with predictions of Fig. 11g, broken fibers were always observed on the bottom side of the L0 specimens.

For L1 laminate, triggering failure mechanisms were similar to those seen in laminate L0. At 99% of the maximum load, the s_{FC} parameter was equal to one along the contact surface between the sample and the nose in the first ply of the laminate (refer to Fig. 13a). Meanwhile, the s_{IMT} parameter progressively approached one at the edges of the contact region (refer to Fig. 13b), indicating that the initial failure resulted from combined fiber failure in compression and in-plane matrix crushing. After the first degradation, failure proceeded differently in the two portions of the beam separated by the rubber layer. In the upper part, as documented by contours of Fig. 13 c and d, fiber failure in compression and in-plane matrix crushing progressively eroded the stiffness of PCM in plies 1–3. Moreover, a symmetric region within PCM having an s_{FT} parameter of one emerged in the upper part of the beam in plies 7 and 8 near the elastomeric film (Fig. 13e). In the lower part of the beam (Fig. 13d), a pronounced area with $s_{IMT} = 1$ triggered in-plane matrix cracking at the interface with the EL film (plies 9 and 10). Additionally, a portion of this region was affected by fiber failure in compression, as depicted in Fig. 13c. In subsequent stages, the various failure mechanisms and resulting stiffness reduction of the PCM material distorted the elements of the rubber film, leading to convergence issues. The last step with acceptably distorted elements highlights that fiber failure in compression combined with in-plane matrix crushing degraded most of the thickness of the upper part

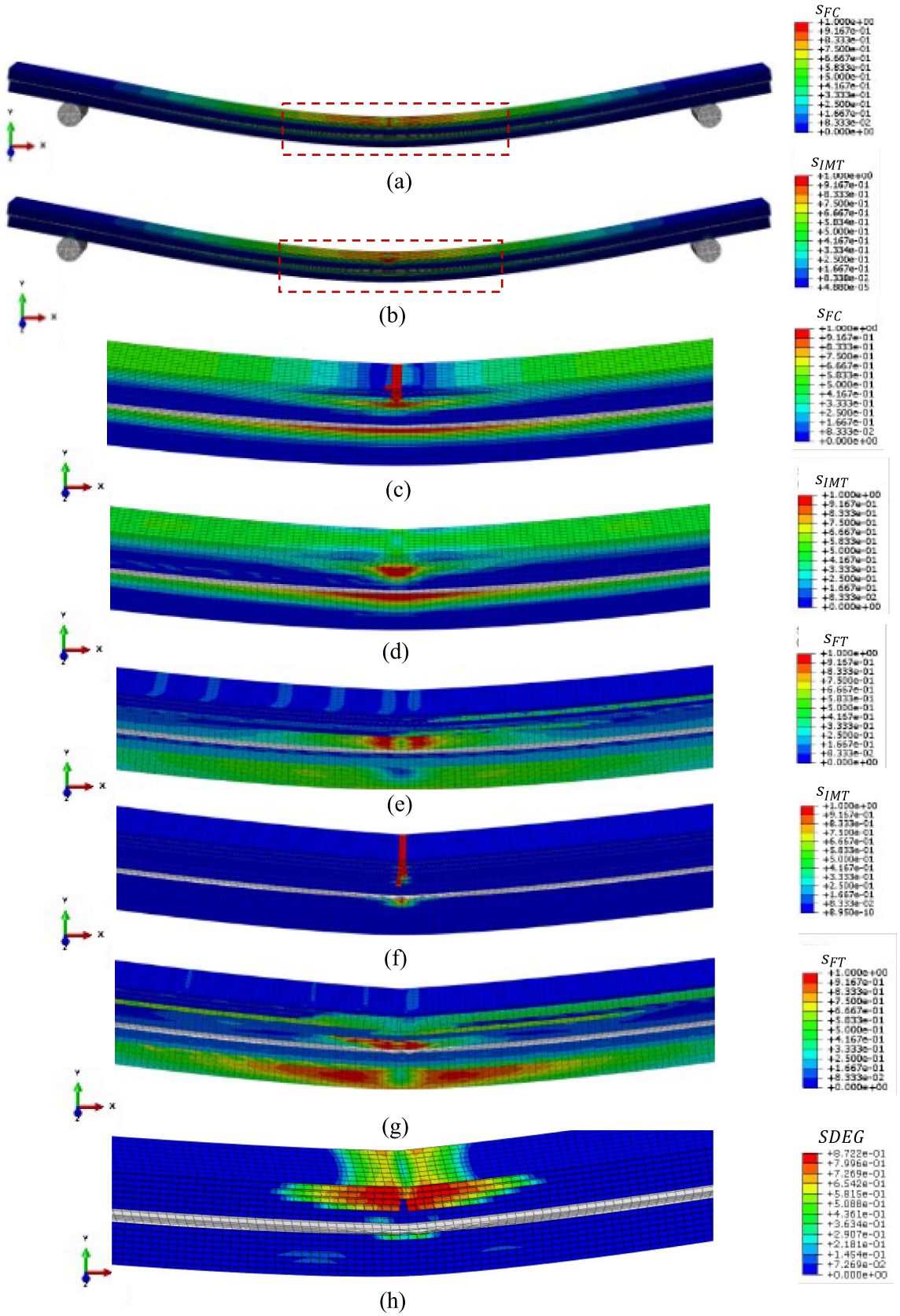
S_{FC}
(a)
S_{IMT}
(b)
S_{FC}
(c)
S_{IMT}
(d)
S_{FT}
(e)
S_{IMT}
(f)
S_{FT}
(g)
$SDEG$
(h)

◂**Fig. 13** Failure initiation and damage progression for L1 laminate. **a** Contour for s_{FC} (fiber compression) at 99% of ultimate load, **b** contour for s_{IMT} (in-plane matrix cracking) at 99% of ultimate load, **c** contour for s_{FC} (fiber compression) after failure, **d** contour for s_{IMT} (in-plane matrix cracking) after failure, **e** contour for s_{FT} (fiber tensile) after failure, **f** contour for s_{IMT} (in-plane matrix cracking) after complete degradation, **g** contour for s_{FT} (fiber tensile) after complete degradation, **h** contour for degradation due to interlaminar damage (SDEG = 0, no damage; SDEG = 1, fully damaged)

of the beam (Fig. 13f), while the remaining part failed for fiber tensile (Fig. 13g) in plies 12–16. Additionally, it can be observed from Fig. 13g that the external fibers of the lower part of the beam (ply 16) are failing in tensile. Delamination was foreseen to occur at first in the highest part of the beam, while initial damage was detected in the lower part, as documented by Fig. 13h. All physical samples from laminate L1 catastrophically failed.

Images from optical microscopy of a representative tested sample captured at the midspan of the specimen are illustrated in Fig. 14. On the upper surface (Fig. 14a), both fractured sides of the sample highlight the presence of crushed fiber in the form of emerging tows. Also for this laminate, outer zones from the fractured areas in Fig. 14a exhibited a permanent deformation, attributed to in-plane matrix cracking. The lateral surface of fractured samples (Fig. 14b) revealed the presence of crushed fibers as well as delaminations. While accurately comparing simulation and experimental results poses challenges, particularly because the numerical simulation ceased prior to the complete separation of the specimen into two parts, notable similarities between the numerical and experimental outcomes are clearly observable. In FEA, the onset of damage and propagation was due to the presence of matrix cracking and fiber failure in compression; both these failure modes are visible in micrographs in the same location predicted by the numerical model. FEA results regarding the initiation of failure and the progression of damage within the L2 laminate are presented in Fig. 15. The in-plane matrix cracking was anticipated in the vicinity of the rubber interlayer located in the upper section of the beam (plies 3 and 4), as evident from Fig. 15 a and b. Moreover, Fig. 15c illustrates the onset of fiber failure in compression ($s_{FC} = 1$) in ply 4 at the boundary between the EL film and the composite material over an extended longitudinal area.

Regions showing initial signs of in-plane matrix crushing ($s_{IMC} = 1$) are observable in ply 11, located in the lower section of the specimen (Fig. 15d) and in proximity to the interface between elastomer and PCM materials. After degradation, as illustrated in Fig. 15e, zones displaying fiber failure in tensile ($s_{FT} = 1$) were observable in both the upper part of the sample (plies 2 and 3) and in the core close to the lower interlayer film (ply 10).

According to the results in Fig. 15f, in-plane matrix cracking ($s_{IMC} = 1$) in proximity to the interface between elastomer and PCM materials was reduced (plies 3–4), while degradation due to fiber compression emerged due to the onset of delaminations (Fig. 15g) in the upper part of the sample localized in plies 10–11. All L2 laminate specimens partially failed due to the toughening action of the EL film that prevented catastrophic damage propagation.

Visible damages for this laminate were consistently observed at the midspan of the tested specimen. Micrographic investigations of Fig. 16, conducted on both the top and side surfaces of a representative specimen, indicated no significant damage due to matrix cracking on the outer surface. Fractures attributed to fiber crushing are markedly visible in Fig. 16b below the upper layer of the rubber film and at the outer fibers of the sample (Fig. 16 a and b). A kinked band region, highlighted in blue in Fig. 16b, was noticed, suggesting that an intense out-of-plane shear deformation

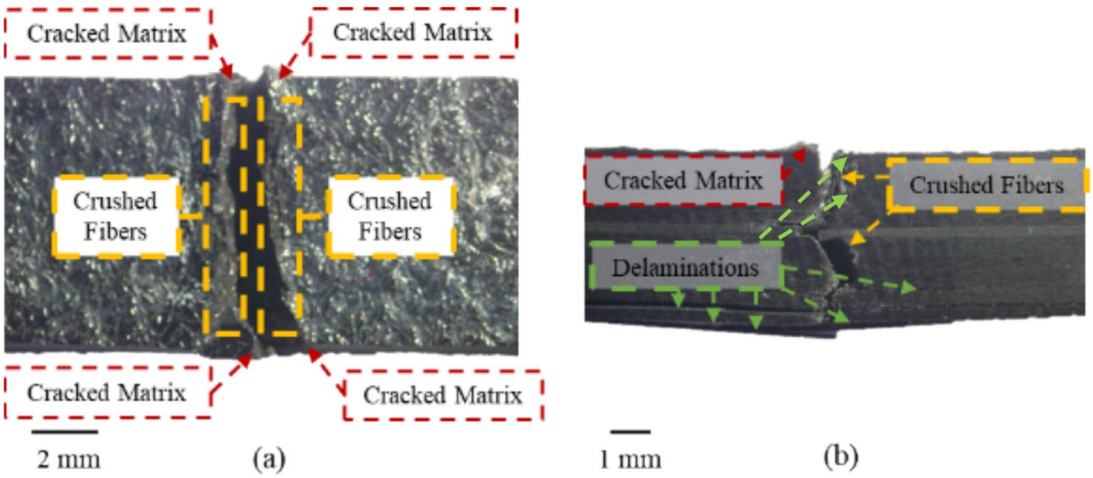

Fig. 14 Surfaces of an L1 sample at the midpoint between loading supports. **a** Top surface, **b** lateral surface

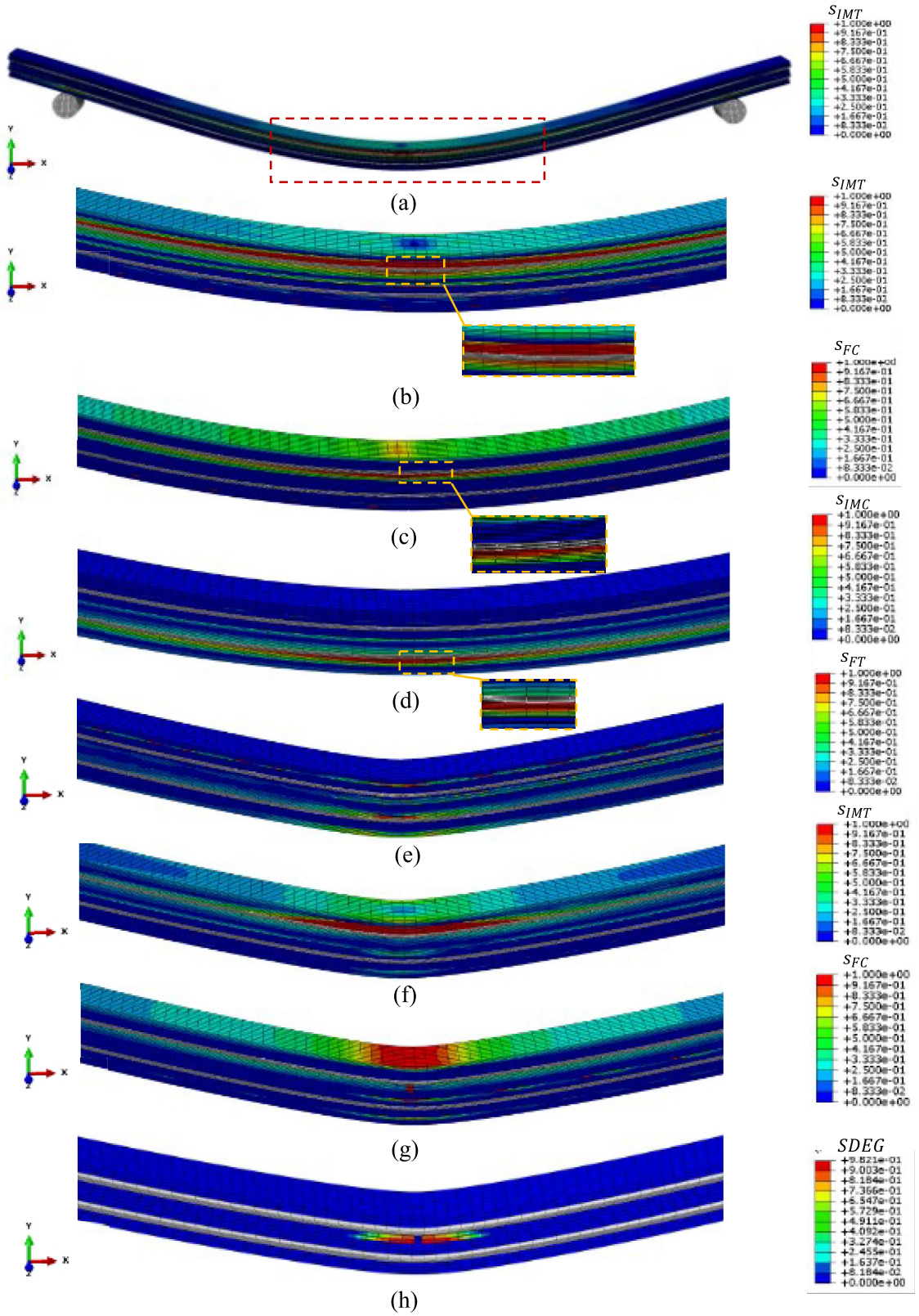

Fig. 15 Failure initiation and damage progression for L2 laminate. **a** Contour for s_{IMT} (in-plane matrix cracking) at 99% of ultimate load, **b** magnification contour for s_{IMT} (in-plane matrix cracking) at 99% of ultimate load, **c** contour for s_{FC} (fiber compression) at 99% of ultimate load, **d** contour for s_{IMT} (in-plane matrix crushing) at 99% of ultimate load, **e** contour for s_{FT} (fiber tensile) after failure, **f** contour for s_{IMT} (in-plane matrix cracking) after failure, **g** contour for s_{FC} (fiber compression) after failure, **h** contour for degradation due to interlaminar damage (SDEG = 0, no damage; SDEG = 1, fully damaged)

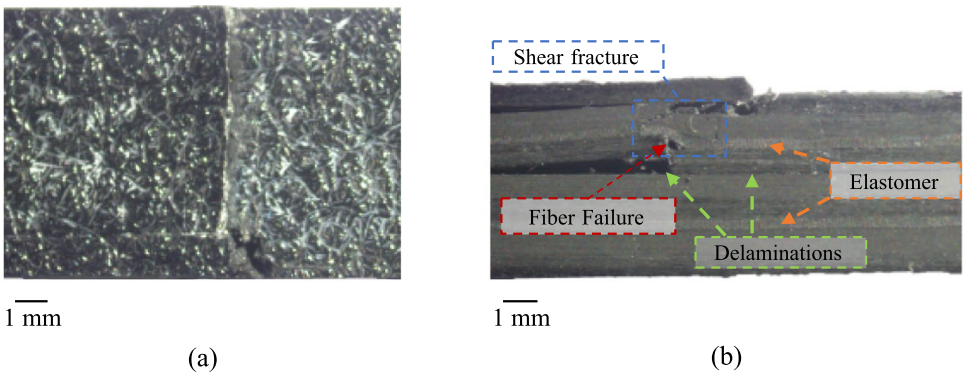

Fig. 16 Surfaces of an L2 sample at midspan. **a** Top surface, **b** lateral surface

caused the relative movement of the plies. It can be argued that in the initial stage, the plies under the upper layer of the EL film failed in compression, causing vast delamination and vertical slippage of material. The interlayer was able to absorb the deformation and hinder the dispersion of PCM debris, demonstrating excellent adhesion properties. Experimental findings are highly consistent with numerical ones, definitively validating the capability of the numerical model to predict damage onset and evolution. No damage initiation or failure was observed in FEA for laminate L3, with all 6 failure parameters (s_{FT}, s_{FC}, s_{IMT}, s_{IMC}, s_{OMT}, and s_{OMC}) consistently below unity at the maximum displacement approached in experimental tests.

4 Conclusions

The effects of integrating different numbers and positions of EL films into CFRP structures were experimentally and numerically demonstrated in this work, enabling a detailed understanding of their impact on the variation of flexural and fracture properties at both local and global levels. By strategically embedding different numbers of EL films in tailored positions, it was possible to tune the material characteristics, resulting in customized performance outcomes. Digital image correlation (DIC) and finite element analysis (FEA) results revealed that this tunability was possible thanks to the extreme shear deformability of the rubber interlayer, which contributes to effectively decoupling the CFRP layers. The peel stresses at the upper and lower edges of the EL interlayer generated distinct damage initiation and evolution modes within the CFRP material, depending on their positioning. The proposed numerical framework, based on Marlow's model, Hashin failure criteria, exponential degradation, and cohesive zone modeling (CZM), proved to be a valuable tool for investigating loading, damage onset, and propagation in HyPCM laminates. Damage onset was validated by comparing experimental stress–strain curves and numerical predictions, showing that the model's predictions fell within the range of experimental variability. Optical microscopy analysis conducted on post-mortem specimens confirmed the accuracy of the results. This framework demonstrated reduced mesh dependency and did not require calibration of any parameters, offering insights that can enhance the design and performance of composite materials. The proposed modeling approach could greatly benefit the design of high-performance composite structures if combined with other established techniques [65]. Although the numerical framework was validated under quasistatic loading, it is believed that the proposed methodology has the potential for broader application to different loading configurations, which will be explored in future work. Furthermore, upcoming research will center on using the framework to determine the optimal thickness and positioning of the EL films. This aims to enhance mechanical performance while reducing weight and material usage.

Supplementary Information The online version contains supplementary material available at https://doi.org/10.1007/s00170-025-15023-x.

Funding Open access funding provided by Alma Mater Studiorum - Università di Bologna within the CRUI-CARE Agreement. This work was supported by Ecosystem for Sustainable Transition in Emilia-Romagna Project, funded under the National Recovery and Resilience Plan (NRRP), Mission 04 Component 2 Investment 1.5—NextGenerationEU, Call for tender n. 3277 dated 30 December 2021 Award Number: 0001052 dated 23 June 2022 CUP: B33D21019790006.

Data availability The raw/processed data required to reproduce these findings will be shared on request.

Declarations

Competing interests The authors declare no competing interests.

References

1. Marmol G, Ferreira DP, Fangueiro R (2021) Automotive and construction applications of fiber reinforced composites. Fiber Reinforced Composites, pp 785–819. https://doi.org/10.1016/b978-0-12-821090-1.00009-0
2. Othman R, Ismail NI, Pahmi MAAH, Basri MHM, Sharudin H, Hemdi AR (2019) Application of carbon fiber reinforced plastics in automotive industry: a review. J Mech Manuf 1:144–154
3. Hsissou R, Seghiri R, Benzekri Z, Hilali M, Rafik M, Elharfi A (2021) Polymer composite materials: a comprehensive review. Compos Struct 262:113640. https://doi.org/10.1016/j.compstruct.2021.113640
4. Gupta MK, Singhal V, Rajput NS (2022) Applications and challenges of carbon-fibres reinforced composites: a review. Evergreen 9:682–693. https://doi.org/10.5109/4843099
5. Jackstadt A, Liebig WV, Kärger L (2022) Analytical modeling and investigation of constrained layer damping in hybrid laminates based on a unified plate formulation. Int J Mech Sci 216:106964. https://doi.org/10.1016/j.ijmecsci.2021.106964
6. Sultan JN, McGarry FJ (1973) Effect of rubber particle size on deformation mechanisms in glassy epoxy. Polym Eng Sci 13:29–34. https://doi.org/10.1002/pen.760130105
7. Kostanski LK, Krolikowski W (1985) Polyester resins modified by elastomers. Polimery/Polymers 30:53–7. https://doi.org/10.14314/polimery.1985.053
8. Chikhi N, Fellahi S, Bakar M (2002) Modification of epoxy resin using reactive liquid (ATBN) rubber. Eur Polym J 38:251–264. https://doi.org/10.1016/S0014-3057(01)00194-X
9. Guo X, Xin J, Huang J, Wolcott MP, Zhang J (2019) Preparation and toughening of mechanochemically modified lignin-based epoxy. Polymer (Guildf) 183:121859. https://doi.org/10.1016/j.polymer.2019.121859
10. Barcikowski M, Rybkowska K (2022) Mode II fracture characterization of toughened epoxy resin composites. Int J Fract 234:223–233. https://doi.org/10.1007/s10704-022-00616-4
11. Treviso A, Van Genechten B, Mundo D, Tournour M (2015) Damping in composite materials: properties and models. Compos Part B Eng 78:144–152. https://doi.org/10.1016/j.compositesb.2015.03.081
12. Maccaferri E, Dalle Donne M, Mazzocchetti L, Benelli T, Brugo TM, Zucchelli A et al (2022) Rubber-enhanced polyamide nanofibers for a significant improvement of CFRP interlaminar fracture toughness. Sci Rep 12. https://doi.org/10.1038/s41598-022-25287-y
13. Liu H, Falzon BG, Tan W (2018) Experimental and numerical studies on the impact response of damage-tolerant hybrid unidirectional/woven carbon-fibre reinforced composite laminates. Compos Part B Eng 136:101–118. https://doi.org/10.1016/j.compositesb.2017.10.016
14. Liu H, Falzon BG, Dear JP (2019) An experimental and numerical study on the crush behaviour of hybrid unidirectional/woven carbon-fibre reinforced composite laminates. Int J Mech Sci 164:105160. https://doi.org/10.1016/j.ijmecsci.2019.105160
15. Raimondi L, Brugo TM, Zucchelli A, Donati L (2024) Effects of UD and twill reinforcements in hybrid sheet molding compound laminates. Mater Res Proc 41:523–9. https://doi.org/10.21741/9781644903131-58
16. Dhaliwal GS, Newaz GM (2020) Experimental and numerical investigation of flexural behavior of hat sectioned aluminum/carbon fiber reinforced mixed material composite beam. Compos Part B Eng 182:107642. https://doi.org/10.1016/j.compositesb.2019.107642
17. Massarwa E, Emami Tabrizi I, Yildiz M (2021) Mechanical behavior and failure of glass/carbon fiber hybrid composites: multiscale computational predictions validated by experiments. Compos Struct 260:113499. https://doi.org/10.1016/j.compstruct.2020.113499
18. Acosta JD, Idarraga G, Maimí P, Jalalvand M, Meza JM (2024) Numerical modelling of multi-directional thin-ply carbon/glass hybrid composites with open holes under tension. Mech Mater 190:104921. https://doi.org/10.1016/j.mechmat.2024.104921
19. Ahmed S, Zheng X, Zhang D, Yan L (2020) Impact response of carbon/Kevlar hybrid 3D woven composite under high velocity impact: experimental and numerical study. Appl Compos Mater 27:285–305. https://doi.org/10.1007/s10443-020-09809-3
20. Del Bianco G, Giammaria V, Capretti M, Boria S, Lenci S, Ciardiello R et al (2024) Low-velocity impact of carbon, flax, and hybrid composites: performance comparison and numerical modeling. Compos Struct 344:118318. https://doi.org/10.1016/j.compstruct.2024.118318
21. Li X, Liu P, Cheng H, Liu C, Zhu Y, Zhang K (2023) Experimental and numerical analysis of low-velocity impact damage of CFRP laminates with negative Poisson ratio (NPR) rubber protective layer. Thin-Walled Struct 191:111066. https://doi.org/10.1016/j.tws.2023.111066
22. Li Z, Zhang J, Jackstadt A, Kärger L (2022) Low-velocity impact behavior of hybrid CFRP-elastomer-metal laminates in comparison with conventional fiber-metal laminates. Compos Struct 287:115340. https://doi.org/10.1016/j.compstruct.2022.115340
23. Albayrak M, Kaman MO, Bozkurt I (2023) The effect of lamina configuration on low-velocity impact behaviour for glass fiber/rubber curved composites. J Compos Mater 57:1875–1908. https://doi.org/10.1177/00219983231164950
24. MacCaferri E, Mazzocchetti L, Benelli T, Brugo TM, Zucchelli A, Giorgini L (2022) Self-assembled NBR/nomex nanofibers as lightweight rubbery nonwovens for hindering delamination in epoxy CFRPs. ACS Appl Mater Interfaces 14:1885–1899. https://doi.org/10.1021/acsami.1c17643
25. Falaschetti MP, Rondina F, Maccaferri E, Mazzocchetti L, Donati L, Zucchelli A et al (2023) Improving the crashworthiness of CFRP structures by rubbery nanofibrous interlayers. Compos Struct 311:116845. https://doi.org/10.1016/j.compstruct.2023.116845
26. Stelldinger E, Kühhorn A, Kober M (2016) Experimental evaluation of the low-velocity impact damage resistance of CFRP tubes with integrated rubber layer. Compos Struct 139:30–35. https://doi.org/10.1016/j.compstruct.2015.11.069
27. Fasana A, Ferraris A, Polato DB, Airale AG, Carello M (2019) Composite and damping materials characterization with an application to a car door. Mech Mach Sci 68:174–184. https://doi.org/10.1007/978-3-030-03320-0_19
28. Proietti A, Gallo N, Bellisario D, Quadrini F, Santo L (2022) Damping behavior of hybrid composite structures by aeronautical technologies. Appl Sci 12:7932. https://doi.org/10.3390/app12157932
29. Povolo M, Raimondi L, Brugo TM, Pagani A, Comand D, Pirazzini L et al (2018) Design and manufacture of hybrid aluminum/composite co-cured tubes with viscoelastic interface layer. Procedia Struct Integr 12:196–203. https://doi.org/10.1016/j.prostr.2018.11.095
30. Raimondi L, Tomesani L, Zucchelli A (2024) Enhancing the robustness of hybrid metal-composite connections through 3D printed micro penetrative anchors. Appl Compos Mater. https://doi.org/10.1007/s10443-024-10224-1
31. Mader A, Born L, Körner A, Schieber G, Masset PA, Milwich M et al (2020) Bio-inspired integrated pneumatic actuation for compliant fiber-reinforced plastics. Compos Struct 233:111558. https://doi.org/10.1016/j.compstruct.2019.111558

32. Born L, Körner A, Mader A, Schieber G, Milwich M, Knippers J et al (2019) Adaptive FRP structures for exterior applications. Adv Mater Lett 10:913–918. https://doi.org/10.5185/amlett.2019.0029
33. Moleiro F, Correia VMF, Araújo AL, Soares CMM, Ferreira AJM, Reddy JN (2019) Deformations and stresses of multilayered plates with embedded functionally graded material layers using a layerwise mixed model. Compos Part B Eng 156:274–291. https://doi.org/10.1016/j.compositesb.2018.08.095
34. Qin H, Yan Y, Liu H, Liu J, Zhang YW, Liu Y (2020) Modified Timoshenko beam model for bending behaviors of layered materials and structures. Extrem Mech Lett 39:100799. https://doi.org/10.1016/j.eml.2020.100799
35. Slesarenko V, Rudykh S (2017) Microscopic and macroscopic instabilities in hyperelastic fiber composites. J Mech Phys Solids 99:471–482. https://doi.org/10.1016/j.jmps.2016.11.002
36. Sadowski T, Golewski P, Craciun E (2021) Internal structure influence on the impact strength and dynamic fracture toughness of hybrid polymer matrix composites with integrated elastomer interlayers. Compos Struct 258:113375. https://doi.org/10.1016/j.compstruct.2020.113375
37. Tsai SW, Wu EM (1971) A general theory of strength for anisotropic materials. J Compos Mater 5:58–80. https://doi.org/10.1177/002199837100500106
38. Hashin Z, Rotem A (1973) A fatigue failure criterion for fiber reinforced materials. J Compos Mater 7:448–464. https://doi.org/10.1177/002199837300700404
39. Pinho ST, Iannucci L, Robinson P (2006) Physically-based failure models and criteria for laminated fibre-reinforced composites with emphasis on fibre kinking: part I: development. Compos Part A Appl Sci Manuf 37:63–73. https://doi.org/10.1016/j.compositesa.2005.04.016
40. Puck A, Schürmann H (2004) Failure analysis of FRP laminates by means of physically based phenomenological models. Failure Criteria in Fibre-Reinforced-Polymer Composites, pp 832–76. https://doi.org/10.1016/B978-008044475-8/50028-7
41. Li X, Li Y, Li F, Huang Z, Chen H (2023) Failure analysis and experimental study on bolted composite joints based on continuum damage mechanics. Compos Struct 303:116274. https://doi.org/10.1016/j.compstruct.2022.116274
42. Linde P, de Boer H (2006) Modelling of inter-rivet buckling of hybrid composites. Compos Struct 73:221–228. https://doi.org/10.1016/j.compstruct.2005.11.062
43. El Idrissi H, Seddouki A (2023) A comprehensive study of the flexural behaviour and damage evolution of composite laminates using a progressive failure model. Int J Adv Manuf Technol 127:3869–3890. https://doi.org/10.1007/s00170-023-11746-x
44. Yang Y, Liu X, Wang YQ, Gao H, Li R, Bao Y (2017) A progressive damage model for predicting damage evolution of laminated composites subjected to three-point bending. Compos Sci Technol 151:85–93. https://doi.org/10.1016/j.compscitech.2017.08.009
45. Huang L, Tao Y, Sun J, Zhang D, Zhao J (2023) Assessment of numerical modeling approaches for thin composite laminates under low-velocity impact. Thin-Walled Struct 191:111053. https://doi.org/10.1016/j.tws.2023.111053
46. ASTM (2014) Astm D3039/D3039M. Annu B ASTM Stand 1–13. https://doi.org/10.1520/D3039
47. ASMT (2013) ASTM D3518 In-plane shear response of polymer matrix composite materials by tensile test of +-45 deg laminate. ASTM Int 641–642:583–90
48. Reu P (2015) All about speckles: speckle density. Exp Tech 39:1–2. https://doi.org/10.1111/ext.12161
49. Reu P (2014) All about speckles: speckle size measurement. Exp Tech 38:1–2. https://doi.org/10.1111/ext.12110
50. Specimens P, Materials EI (2011) Standard test methods for flexural properties of unreinforced and reinforced plastics and electrical insulating materials 1–11. https://doi.org/10.1520/D0790-10
51. McCarthy CT, McCarthy MA, Stanley WF, Lawlor VP (2005) Experiences with modeling friction in composite bolted joints. J Compos Mater 39:1881–1908. https://doi.org/10.1177/0021998305051805
52. Xu W, Jiang D, Zhang C, Li H, Qiang S, Li Y et al (2023) An adaptive mesh refinement strategy for 3D phase modeling of brittle fracture. Eng Fract Mech 284:109241. https://doi.org/10.1016/j.engfracmech.2023.109241
53. Nguyen-Xuan H, Liu GR, Bordas S, Natarajan S, Rabczuk T (2013) An adaptive singular ES-FEM for mechanics problems with singular field of arbitrary order. Comput Methods Appl Mech Eng 253:252–273. https://doi.org/10.1016/j.cma.2012.07.017
54. Kachanov LM (1999) Rupture time under creep conditions. Int J Fract 97:11–18. https://doi.org/10.1023/a:1018671022008
55. Bažant ZP, Oh BH (1983) Crack band theory for fracture of concrete. Matériaux Constr 16:155–177. https://doi.org/10.1007/BF02486267
56. Rondina F, Donati L (2020) Comparison and validation of computational methods for the prediction of the compressive crush energy absorption of CFRP structures. Compos Struct 254:112848. https://doi.org/10.1016/j.compstruct.2020.112848
57. Marlow RS (2003) A general first-invariant hyperelastic constitutive model. In: Constitutive Models for Rubber III. CRC Press, pp 157–160
58. Camanho PP, Dávila CG, De Moura MF (2003) Numerical simulation of mixed-mode progressive delamination in composite materials. J Compos Mater 37:1415–1438. https://doi.org/10.1177/0021998303034505
59. Giuliese G, Palazzetti R, Moroni F, Zucchelli A, Pirondi A (2015) Cohesive zone modelling of delamination response of a composite laminate with interleaved nylon 6,6 nanofibres. Compos Part B Eng 78:384–392. https://doi.org/10.1016/j.compositesb.2015.03.087
60. Benzeggagh ML, Kenane M (1996) Measurement of mixed-mode delamination fracture toughness of unidirectional glass/epoxy composites with mixed-mode bending apparatus. Compos Sci Technol 56:439–449. https://doi.org/10.1016/0266-3538(96)00005-X
61. Rondina F, Falaschetti MP, Zavatta N, Donati L (2023) Numerical simulation of the compression crushing energy of carbon fiber-epoxy woven composite structures. Compos Struct 303:116300. https://doi.org/10.1016/j.compstruct.2022.116300
62. Palanca M, Brugo TM, Cristofolini L (2015) Use of digital image correlation to investigate the biomechanics of the vertebra. J Mech Med Biol. https://doi.org/10.1142/s0219519415400047
63. Raimondi L, Brugo TM, Zucchelli A (2021) Fiber misalignment analysis in PCM-UD composite materials by full field nodal method. Compos Part C Open Access 5:100151. https://doi.org/10.1016/j.jcomc.2021.100151
64. Badrul Hasan MM, Nitsche S, Abdkader A, Cherif C (2019) Influence of process parameters on the tensile properties of DREF-3000 friction spun hybrid yarns consisting of waste staple carbon fiber for thermoplastic composites. Text Res J 89:32–42. https://doi.org/10.1177/0040517517736472
65. Cocchi D, Raimondi L, Brugo TM, Zucchelli A (2020) A systematic material-oriented design approach for lightweight components and the CFRP motor wheel case study. Int J Adv Manuf Technol 109:2133–2153. https://doi.org/10.1007/s00170-020-05756-2